Physics of chromatic focusing, post-acceleration and bunching of laser-driven proton beams in helical coil targets

M Bardon, J Moreau, L Romagnani, C Rousseaux, M Ferri, F Lefévre, I Lantuéjoul, B Etchessahar, S Bazzoli, D Farcage, et al.

▶ **To cite this version:**

M Bardon, J Moreau, L Romagnani, C Rousseaux, M Ferri, et al.. Physics of chromatic focusing, post-acceleration and bunching of laser-driven proton beams in helical coil targets. Plasma Physics and Controlled Fusion, 2020, 62 (12), pp.125019. 10.1088/1361-6587/abbe35 . hal-03046046

HAL Id: hal-03046046
https://hal.science/hal-03046046

Submitted on 12 Aug 2021

HAL is a multi-disciplinary open access archive for the deposit and dissemination of scientific research documents, whether they are published or not. The documents may come from teaching and research institutions in France or abroad, or from public or private research centers.

L'archive ouverte pluridisciplinaire **HAL**, est destinée au dépôt et à la diffusion de documents scientifiques de niveau recherche, publiés ou non, émanant des établissements d'enseignement et de recherche français ou étrangers, des laboratoires publics ou privés.

Physics of the chromatic focusing, post-acceleration and bunching of laser driven ion beams in helical coil targets

M. Bardon,[1, a)] J. G. Moreau,[1] L. Romagnani,[2] C. Rousseaux,[3] M. Ferri,[1] F. Lefèvre,[2] I. Lantuejoul,[3] B. Etchessahar,[1] S. Bazzoli,[3] D. Farcage,[4] H. Maskrot,[4] F. Serres,[2] M. Chevrot,[2] E. Loyez,[2] E. Veuillot,[2] W. Cayzac,[3] B. Vauzour,[3] G. Boutoux,[3] G. Sary,[3] A. Compant La Fontaine,[3] L. Gremillet,[3] A. Poyé,[5] E. D'Humières,[6] and V. T. Tikhonchuk[6, 7]

[1)] *CEA-CESTA, Le Barp F-33114, France*

[2)] *LULI, CNRS-Ecole Polytechnique-CEA-Université Paris VI, Palaiseau F-91128, France*

[3)] *CEA-DIF, Bruyères-le-Châtel F-91297, France*

[4)] *CEA-Saclay, Gif-sur-Yvette F-91191, France*

[5)] *Aix-Marseille Université, CNRS, PIIM, UMR 7345, Marseille F-13397, France*

[6)] *CELIA, University of Bordeaux-CNRS-CEA, Talence F-33405, France*

[7)] *ELI-Beamlines, Institute of Physics CAS, Dolní Břežany 25241, Czech Republic*

To increase the fluence and the maximum energy of laser driven ion beams in view of potential applications such as isochoric heating of dense material or isotope production, it has been proposed to attach a helical coil normally to the rear side of the irradiated target. By driving the target discharge current pulse through the coil, this scheme allows to focus, post-accelerate and select in energy a part of the ion beam. The previously published results are extended to higher laser pulse energies and longer coils. This leads to an increased number of guided protons and the generation of several proton bunches. Large scale particle-in-cell simulations with realistic boundary conditions reproduce well the experimental results. A detailed analysis of the numerical simulations and an analytical model demonstrate the crucial role of the discharge current pulse dispersion in the proton bunch trapping and focusing.

I. INTRODUCTION

Since the 2000s, ion acceleration by intense and short laser pulses[1,2] has become an intense research field due to many promising applications such as isochoric heating[3], isotope[4] or neutron[5] production, plasma radiography[6,7], ion driven fast ignition[8,9], and tumor therapy[10]. The laser generated ion beams present interesting properties such as low emittance, short pulse duration, high current, high laminarity and high brightness. Among all the ion acceleration mechanisms, the Target Normal Sheath Acceleration (TNSA)[11,12] is the most robust process. Here, the ions are accelerated by TV/m sheath electric fields created by the laser heated and recirculating electrons, from the rear side of a thin solid foil. However, these ion beams have a large divergence angle ($\sim 40°$), energy bandwidth (exponential distribution) and their maximum energy strongly depends on the laser intensity.

To overcome these limitations, numerous upgraded schemes have been designed to collimate, select in energy and post-accelerate the ion beam emitted from the rear side of the irradiated target. Static methods consist of using curved (rear side) targets, hemispheres or microstructured targets[3,12–19] or injecting the TNSA produced ions in a permanent magnetic quadrupole[20–22] or pulsed solenoid[23,24]. Other methods dynamically control the focusing and possibly the energy selection of the ions emitted from the rear side of the target. The authors of Ref. 25 use a cylinder irradiated by a second laser pulse so that the laser generated protons are focused by the strong radial electrostatic field (TV/m) produced inside the cylinder. Control of the time delay between the two laser pulses allows energy selection of the focused protons in this microlens. Another alternative is to inject the laser-produced ions in a radio frequency-based accelerator or a beam transport device[26–29].

Kar et al.[30] proposed to attach a helical coil normally to the rear side of the irradiated target foil so that the generated TNSA ions propagate along the helix axis. This structure has an advantage of producing, collimating, energy selecting and post accelerating the ion beam. It also benefits from an "all-optical approach"[30], because a single intense laser pulse is needed to produce the ion beam and to trigger the ion focusing and post-acceleration, without any extra driver.

This multi-physics and multi-scale process can be summarized as follows. During the interaction of a relativistic laser pulse with a target, hot electrons are produced[31] and start to escape from it. The target potential rises with time to a megavolt level and prevents more electrons to escape[32–34]. At the same time, an ion beam is produced at the rear side of the target by the TNSA mechanism[11,12]. Escaping hot electrons are charging positively the target, and a short discharge current pulse is generated at the same time with the ion acceleration. This current pulse propagates along the wire turned into a helix[30,35–38] and generates an electromagnetic pulse

[a)] Electronic mail: matthieu.bardon@protonmail.com

(EMP)[39,40] which focuses, post-accelerates and energy selects the ions. The helix plays a double role of an electromagnetic field guide and delay line for the discharge current pulse. Such a structure is commonly used in radio-frequency accelerators[41,42] and travelling wave tubes[43].

The effectiveness of this structure has been demonstrated in a proof-of-principle experiment[30] using a ~ 30 fs duration ~ 3 J energy laser pulse focused at peak intensity of a few 10^{20} W cm^{-2} on a thin gold foil with a helical coil $L = 7.8$ mm long and $a = 0.4$ mm radius attached to the rear side of the target. It has been tested also with longer (~ 600 fs) laser pulses of similar energy ($\sim 5-7$ J) and shorter helical coils ($L = 1.8$ to 5.5 mm) in Refs. 35, 44, and 45.

The phenomenology of the ion focusing and post-acceleration in a helix has been studied in numerical simulations but the set-up was not sufficiently representative. Jiang et al.[46] used Particle-In-Cell (PIC) simulations to simulate the interaction of the laser pulse with a micrometric-scale and fully ionized target and a helical coil. This setup cannot be applied to a conducting, millimetric-scale, and non-ionized helical wire. Kar et al.[30,35,44] used test particle simulations[47] of the proton focusing and post-acceleration by the electric field generated by a charged ring moving along the coil axis. However, the charged ring has a prescribed shape and propagates with a constant velocity along the wire. The velocity $v \approx 0.96c \pm 0.04c$ was deduced from the analysis of a proton probing experiment of the electromagnetic pulse propagation along a folded wire. By contrast, in this article we show that the current propagation along a helical wire is different from the propagation in a linear or a folded wire. The current pulse propagation along a helical wire is subjected to a velocity dispersion and results in a modification of the current pulse shape.

We report here on the study of proton acceleration with laser pulses of a high energy (40 J after compression compared to 7 J in Ref. 44) and with long helical structures (from 8 to 15 mm). It is shown that the holder of the target and the helical wire must be carefully designed to prevent a short-circuit. The performances of the helical structure are analyzed with three-dimensional (3D) large scale PIC simulations using realistic boundary conditions for the helical wire modeled at the real scale[48]. Numerical simulations are in good agreement with the experimental results. They demonstrate that a discharge current pulse propagates through the helical wire and generates an electromagnetic pulse (EMP), which affects on the protons dynamics. As the intrinsic inductance and capacitance of the helical structure depend on the frequency[49], the discharge current pulse is subject to dispersion, which affects its propagation velocity along the helix axis and has a strong impact on the proton bunching. The current pulse dispersion is illustrated with an analytical model derived from the traveling wave tube theory[43,49], which is in good agreement with the numerical simulations.

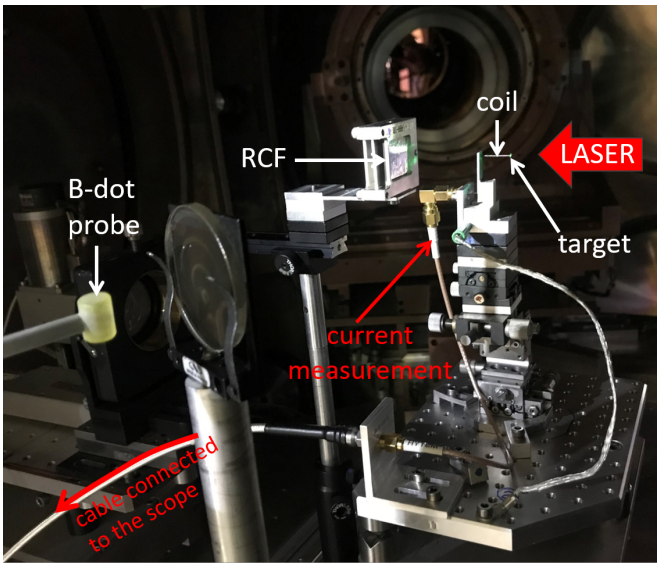

FIG. 1. Experimental set-up.

This paper is structured as follows. Section II presents the set-up and the results of the experimental campaign carried out on the LULI2000 facility. Section III presents numerical simulations of proton acceleration and bunching and their comparison to experimental results. Section IV presents the analysis of evolution of the discharge current during its propagation along the helical wire, observed in the PIC simulations and in the analytical model. Section V summarizes the new phenomena observed in the experimental campaign and the effects of current dispersion on the proton post-acceleration and bunching.

II. EXPERIMENTAL CAMPAIGN

A. Experimental set-up

The experimental campaign was conducted on the LULI2000 facility[50] (Ecole Polytechnique, Paris, France) employing the pico2000 laser delivering a laser pulse at a wavelength $\lambda_l = 1.053$ μm, with energy $E_l = 40 \pm 4$ J on target, and duration $\tau_l = 1.3$ ps. The laser was focused at normal incidence on a 20 μm thick and few mm large gold (Au) foil using a $f/4$ off-axis parabola to a spot of 10 μm full-width at half-maximum (FWHM), leading to peak intensities of the order $I_l \approx 10^{19}$ W cm^{-2}. The laser contrast was 10^{-10} at 1 ns before the main pulse, increasing to $10^{-6.5}$ from 1 ns to 0.5 ns, and remained at this level to 0.08 ns. The residual pressure in the chamber was $\sim 10^{-4}$ mbar.

The experimental set-up is shown in Figure 1. The angular and spectral distributions of the proton beam are diagnosed, with and without the helical structure, by a stack of radiochromic films (RCF) located from 2 to 6 cm

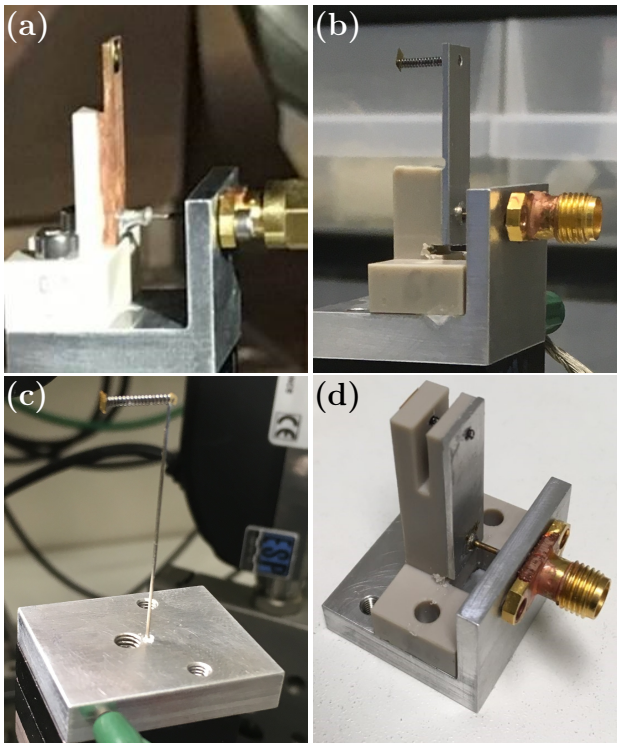

FIG. 2. Set-ups used to hold the target foil alone (a) and the helical coil attached to the rear side of the foil (b, c, d).

behind the foil target. Two 10 μm thick aluminium foils are added at the front of the RCF stack to stop the major part of X-rays and hot electrons. Measurement of the opacity of RCF films gives an absolutely calibrated proton spectrum (see Appendix A for details). The discharge current is measured in several shots with (Figure 2(d)) and without (Figure 2(a)) the helical structure. A B-dot probe is used to measure the magnetic field at a distance of 22.5 cm from the target chamber center (TCC).

During this campaign, several target and holder geometries have been tested. In first series of laser shots, a 20 μm gold foil was attached to a vertical copper strip fixed at a dielectric holder made of PEEK (PolyEther Ether Ketone) (see Figure 2(a)). This target holder geometry allows to guide the discharge current[32] to the ground and is dedicated to the measurement of the discharge current intensity. By integration, we have also accessed to the emitted charge and can control the shot to shot stability.

In other laser shots, a helical wire was attached to the rear side of the gold foil. This helical wire had a shape of a spring, it was manufactured industrially from a 200 μm diameter steel or stainless steel wire. The coil radius was set to $a = 0.5$ mm, the length was varied from $L = 8$ mm to 15 mm and the pitch from $p = 0.35$ mm to 0.45 mm. Three different holders of the coil and target foil have been tested (see Figure 2):

(i) Panel b shows a helical coil maintained at its end by a 1-mm-thick aluminium (Al) vertical strip. This strip guides the discharge current pulse to the ground or the scope. It is supported by a dielectric holder made of PEEK.

(ii) Panel c shows a helical coil maintained at its end by a vertical pin. The other extremity of the pin is connected to the ground.

(iii) Panel d shows a dielectric holder wrapping the helical coil with the Au foil pasted on it. In this much more robust design, the Au foil is perfectly perpendicular to the coil axis and the electric contact between the foil and the coil is insured. This target holder also permits the measurement of the discharge current.

For all these holders, the spectral and angular profiles of protons emitted from the target were measured by a RCF stack.

B. Experimental results and evidence of proton focusing, post-acceleration and energy selection

Figures 3, 4, 5 and 6 present the major effects of the helical structures on the proton beam properties. Figure 3 displays a comparison of the angular and spectral profiles obtained on the RCF stack of the proton beam emitted from the rear side of the foil target (a) and from the end of a helical coil attached to it (b). This helical structure has a pitch $p = 0.45$ mm, a length $L = 8$ mm and it is held at the end by a 1 mm Al strip as shown in Fig. 1(a). The proton profile obtained without the helical coil is common to the TNSA mechanism and features an opening angle $\alpha \approx 40°$ for the lowest energy protons, and $\alpha \approx 20°$ for the 10 MeV protons. Protons with energy $E_p \lesssim 9$ MeV are stopped by the 200 μm diameter stainless helical wire[51]. Therefore, comparisons with and without the helical coil were performed inside the aperture angle of the coil ($\sim 5.7°$) which is represented by the red circle in Fig. 3.

In Figure 3(b), a dark spot much smaller than the coil aperture angle is observed for proton energy greater than 5 MeV. It means that a large proportion of protons with $E_p > 5$ MeV are well focused. This dark spot is still observed for energy of 18 MeV and it is much darker than the one observed without the helical wire. This focusing is quantitatively demonstrated in Fig. 4(a) by a comparison of the maximum fluence measured on each film of the stacks in Fig. 3 as a function of proton energy with (red curve) and without (blue curve) the helical coil. This plot shows, in particular, that the maximum fluence for proton energy $E_p > 10$ MeV is multiplied by a factor $\gtrsim 7$ with the use of the helical coil. This result has been confirmed in several other shots. Figure 4(b) presents a comparison of the corresponding proton spectra with (red curve) and without the helical coil (blue curve). The proton charge with $E_p > 3.5$ MeV is increased from 1.5 nC ($N_p \sim 9 \times 10^9$), without coil, to 3.3 nC ($N_p \sim 2 \times 10^{10}$)

with the coil and that the proton effective temperature T_p (measured as a slope of proton energy spectrum) is increased from 2.9 to 4.8 MeV.

This comparison demonstrates that the helical coil has focused a large number of protons which were not emitted originally in its aperture angle. By considering a short current pulse propagating along the helical wire with the velocity $v_i \approx c$[30,36], one may expect that the collimated protons are the ones which propagate with the same velocity as the current pulse along the coil axis:

$$v_0 = \frac{\beta}{\sqrt{1+\beta^2}}c, \tag{1}$$

where $\beta = p/2\pi a$ is the tangent of the angle of the turns with respect to the helix axis. This velocity corresponds to the proton energy $E_p \approx 9.6$ MeV. However, Figure 4 shows that the energy bandwidth of collimated protons is much larger, it covers the interval from 3.5 to 15 MeV. This is due to the fact that the current pulse does not conserve the initial Gaussian shape while propagating along the helical wire with a constant velocity. By contrast, this pulse is modulated during its propagation, which results in modification of its effective velocity (see Sec. IV).

Another important phenomenon is a halo observed in Figure 3(b) for the smallest proton energies, which is much bigger than the coil aperture. This halo is observed in the great majority of the shots with different holders (including the Al strip holder). We suspect that it is produced by the protons which are focused at a short distance from the coil end and are then defocused, before reaching the RCF stack. This hypothesis will be confirmed in future experiments.

The use of a helical coil with pitch $p = 0.45$ mm and length $L = 8$ mm hold by a pin (see Fig. 2(c)) gives similar results to the ones obtained with an Al strip holder. A proton spectrum measured 3 cm away from the target is plotted in red in Fig. 5 and compared to the proton spectra measured 4 cm from the target without helical coil (blue curves). These proton spectra (obtained in seven laser shots without the coil) are similar, despite small variations of laser energy, duration and focal spot. A comparison shows that the proton temperature has been multiplied by a factor of 4 and the maximum proton energy has been increased by approximately 5 MeV, which then reaches 19.6 MeV. This post-acceleration of the proton beam in the helical coil is also flagged by a comparison of the proton angular and spectral distribution on the RCF stack in Fig. 3.

Figure 6 shows the proton spectrum emitted out of a longer helical coil ($p = 0.35$ mm, $L = 15$ mm) held by an Al strip (see Fig. 2(b)) measured in a 3° cone 6 cm away from the target. It is compared to the proton spectrum measured in a 3° cone 4 cm away from the target without helical coil. This comparison emphasizes two proton peaks around 3 MeV and 10 MeV that are formed with a long helical coil. This is a demonstration

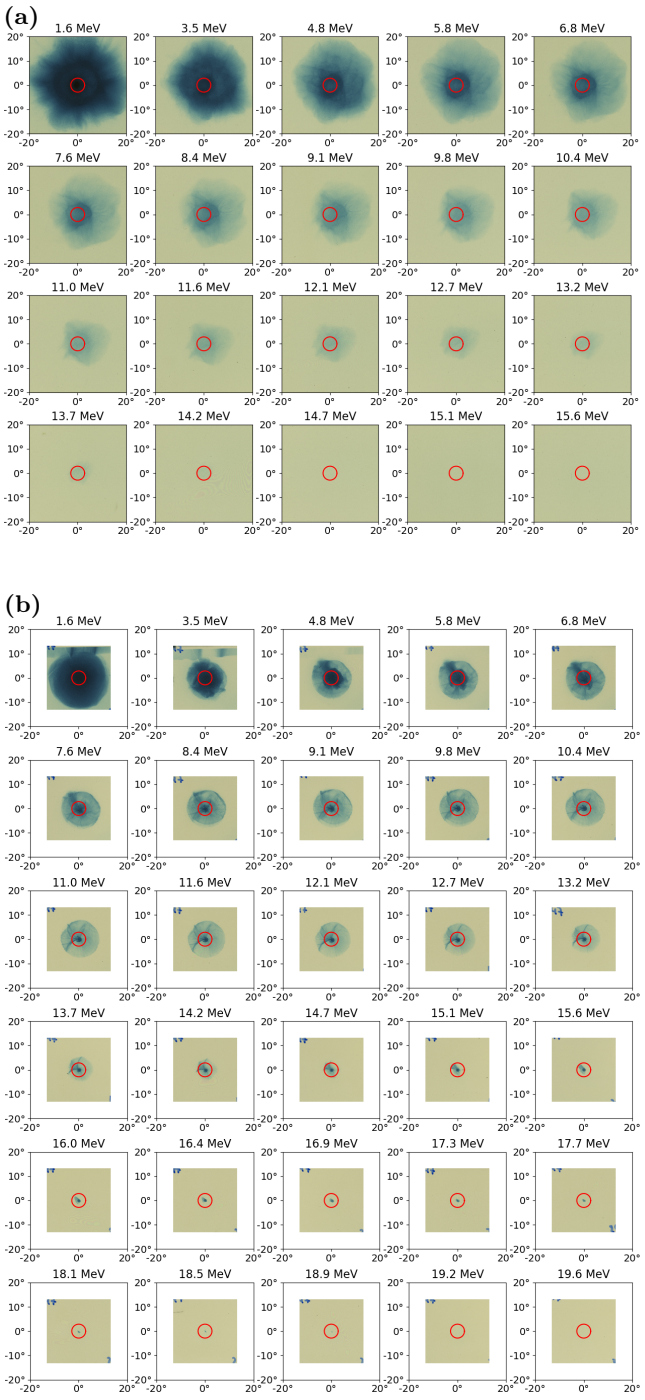

FIG. 3. Comparison of the proton beam profile on the RCF stack obtained without (a) and with (b) the use of a helical coil and measured 4 cm (4.5 cm respectively) away from the Au foil. The helical coil attached to the target rear has a pitch $p = 0.45$ mm and a length $L = 8$ mm. The red circle shows the aperture angle of the coil. The energy written above each RCF corresponds to the energy of protons whose Bragg peak is located at the RCF position in the stack (see Appendix A for details).

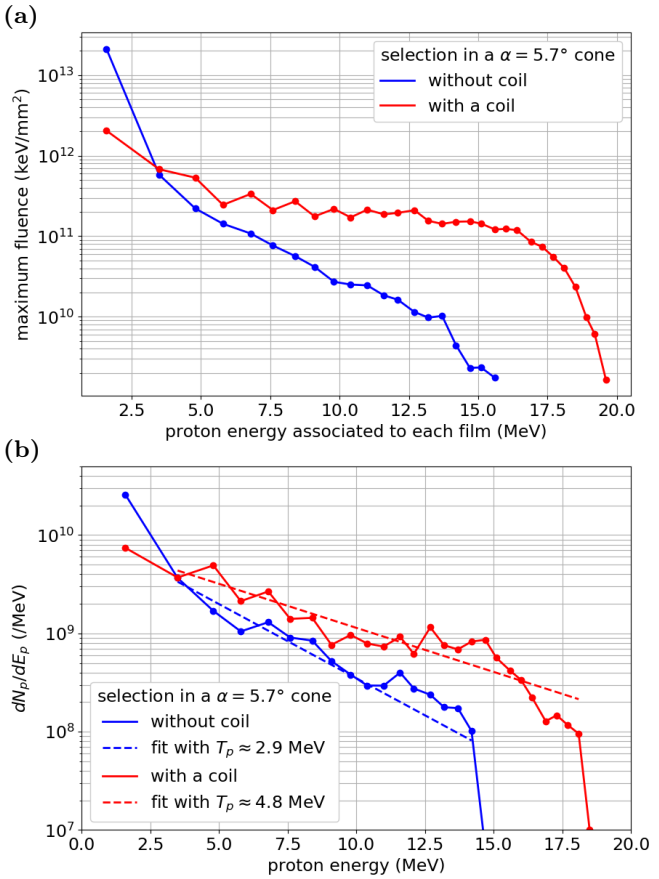

FIG. 4. Comparison of the proton beam maximum fluence (a) and spectra (b) obtained with (red) and without (blue) the helical coil. The helical coil has a pitch $p = 0.45$ mm and a length $L = 8$ mm.

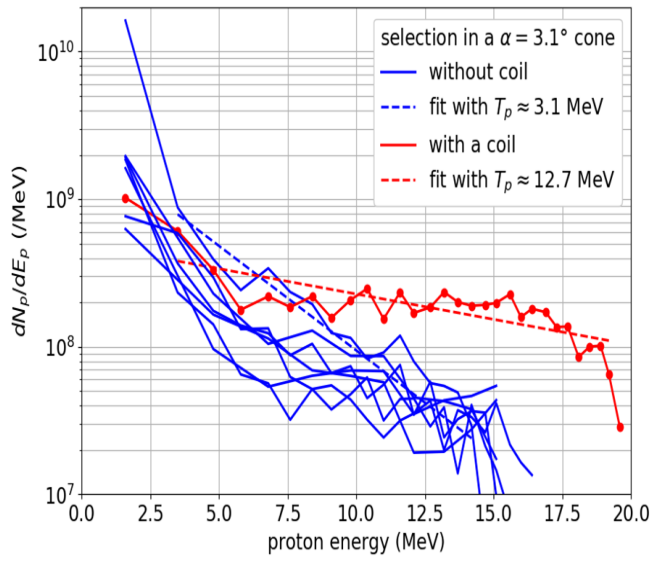

FIG. 5. Comparison of the proton beam spectra obtained with (red) and without (blue) the helical coil. The helical coil has a pitch $p = 0.45$ mm and a length $L = 8$ mm.

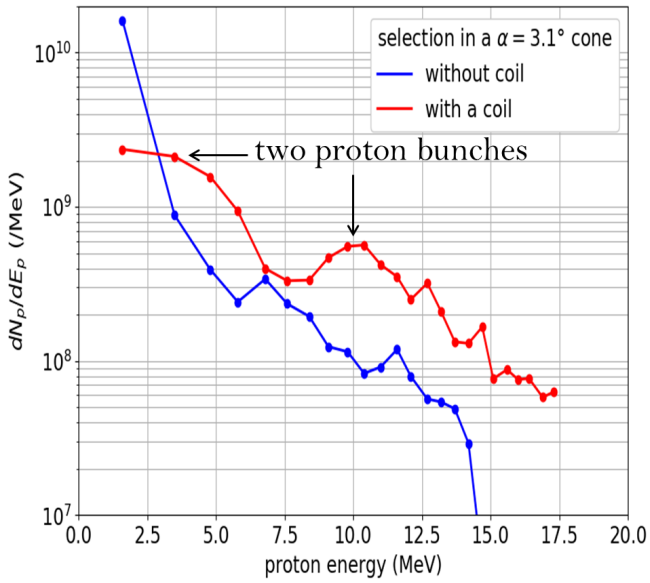

FIG. 6. Comparison of the proton beam spectra obtained with (red) and without (blue) the helical coil. The helical coil has a pitch $p = 0.35$ mm and a length $L = 15$ mm.

of proton bunching of the helical coil, which is further discussed in Sec. III.

These experiments have unambiguously demonstrated the proton focusing, post-acceleration and bunching by a helical coil for a higher laser energy ($E = 70$ J) and a longer coil (between 8 to 15 mm) than the past publications[30,35,44].

C. Impact of the target and helical coil holder in high energy laser experiments

A holder with a helical coil wrapped by the PEEK material (see Fig. 2(d)) was also tested. This holder is very robust and convenient for alignment, but the experiment showed that, despite these advantages, it does not lead to proton focusing or post-acceleration. To understand this difference compared to other holders, the discharge current has been measured. It is plotted in blue in Fig. 7(a) and compared to another laser shot without helical coil. The discharge current is very similar in both cases. This provides evidence that the current does not propagate along the helical coil but passes through the PEEK holder although it is originally an insulator. Our hypothesis is that it is being ionized by x-rays and energetic electrons during the laser target interaction and conducts surface currents. This observation shows that, at a high laser energy, the helical coil holder can have a strong impact on the coil performance and it must be designed with care. In order to avoid such issues, the helical coil must be held at the opposite end of the target.

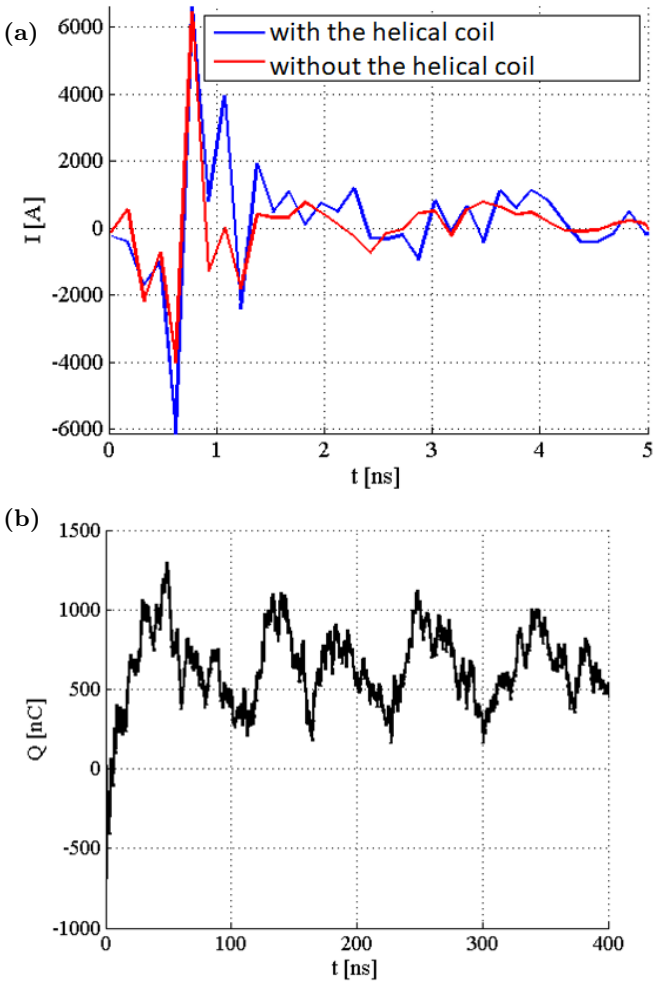

FIG. 7. (a) Discharge current measured at the end of the target holder 2.d with (blue) and without (red) helical coil. (b) Accumulated target charge.

D. Characterization of electron and proton emission from the gold foil target

Experimental results shown above allow us to infer information about emission of electrons and protons from the target. The proton spectra obtained without helical coil plotted in blue in Fig. 5 can be fitted with a Maxwellian function:

$$\mathrm{d}N_p/\,\mathrm{d}E_p = N_0 \exp\left(-E_p/T_p\right) \qquad (2)$$

with the effective temperature $T_p = 3$ MeV and cutoff energy $E_{p,\max} \approx 15$ MeV. Integrating this spectrum over the interval $[1.6, 15]$ MeV gives the total emitted proton charge of the order $Q_p \approx 50$ nC.

According to Figure 7(a), an amplitude and FWHM duration of the discharge current pulse are 6 kA and 100 ps, respectively. The current pulse is modified while propagating through the coil (see Sec. IV) and also through the Al strip, which has an inductance of $30 - 50$ nH. Therefore, the pulse duration observed in

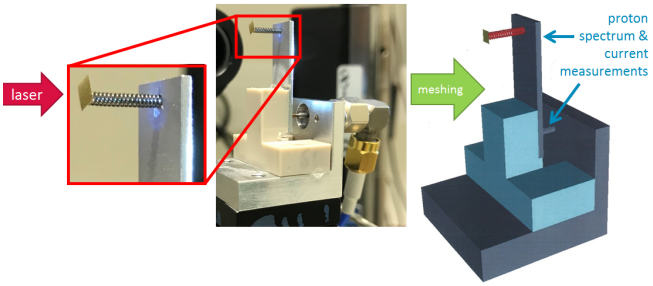

FIG. 8. Target, coil and holder set-up. The meshed part is shown in the red square.

Figure 7 is much longer than the one at the beginning of the coil due to dispersion effects. In Sec. III, we present a method allowing to infer this initial pulse duration. The total charge accumulated on target due to the escaped electrons can be estimated by integrating the discharge current over time, $Q_e = \int_0^t I(t')\,\mathrm{d}t'$. As shown in Figure 7(b), it is of the order of $Q_e \sim 600 - 700$ nC, which is in agreement with the data obtained in other experiments with similar laser pulse parameters[40,52].

III. LARGE SCALE PIC SIMULATIONS

Numerical simulations were conducted with the code Sophie[48] developed at the CEA-CESTA. This 3D PIC code solves, in a dielectric material, the Maxwell's equations for the electromagnetic fields and, in vacuum, the relativistic dynamics equations for electrons and protons along with the Maxwell's equations. The complete target and holder geometry is modeled by appropriate boundary conditions on the conducting surfaces, electrons and protons are ejected from the target surface according to prescribed emission laws. The code simulates the electron and proton dynamics, target charging, discharge current generation and propagation through the helical coil and Al strip self-consistently.

The reference case considers a helical coil ($p = 0.35$ mm, $L = 15$ mm) attached to the rear side of a foil target (see Fig. 6). The target, coil and holder are assumed to be perfect conductors and are meshed in real scale with the cell size $\Delta x = \Delta y = \Delta z = 20$ μm (2×10^9 cells, see Figure 8). The PEEK holder is modeled as a dielectric with permittivity $\varepsilon = 3.2$ and permeability $\mu = 1$. Electrons and protons are modeled with 30 million macroparticles.

Energy and angle distributions of the proton emission are taken from the experiment, from the shots with target foil alone (see Figs. 3(a) and 5). The total charge is $Q_p \approx 50$ nC. The energy distribution is a Maxwellian function (2) with the effective temperature $T_p = 3$ MeV over the interval $[1, 13]$ MeV. The angular distribution $\mathrm{d}N_p/\,\mathrm{d}\theta$ is approximated by a super-Gaussian function centered around $\theta = 0$. Temporal shape of proton emis-

sion $\mathrm{d}N_p/\mathrm{d}t$ is assumed to follow a Gaussian law. Duration of proton ejection (*a priori* a few ps) is experimentally unknown, but it is a insignificant compared to the time of proton propagation along the coil (a few 100 ps), and bunch stretching due to the velocity dispersion. The transverse size of ion emission zone is set to 200 μm, which is of the same order as reported in Refs. 53 and 54.

Proton dynamics inside the helical coil is only governed by electromagnetic fields generated by the discharge current propagating along the coil. Therefore, accurate description of electron emission is necessary in order to reproduce the accurate magnitude and pulse duration of the discharge current in the coil. However, the electron emission characteristics are *a priori* unknown. Only the current intensity at the end of the Al strip and the net charge are measured in the experiment. The input parameters of the simulation have then been set as follows. The size of the electron emission area is set identical to the one of protons (200 μm). The angular distribution is assumed to be isotropic. The spectrum of emitted electrons $\mathrm{d}N_e/\mathrm{d}E_e$ is assumed to follow the same exponential law as protons (2) with temperature $T_e = 3$ MeV and maximum energy $E_{e,\max} = 15$ MeV. The total emitted charge is 600 nC. The rate of electron emission $\mathrm{d}N_e/\mathrm{d}t$ was inferred from a series of simulations. It is assumed to be a Gaussian function with a FWHM varying from $\tau_e = 3$ ps to 60 ps. Proton spectra in a 3° cone obtained in these simulations at the end of the helical coil are compared to the experimental data in Fig. 9. The maximum proton energy in the simulated spectra is in good agreement with the experiment within the error, independently of the chosen electron emission duration. However, the two proton peaks around 3 and 10 MeV observed experimentally only appear in the simulated spectra, if the electron emission duration is less than 15 ps. This time $\tau_e \approx 15$ ps was chosen for the duration of electron emission in all subsequent simulations.

This time is comparable to the one measured in Refs. 30, 36, and 37, where proton beam was used to diagnose transient electric fields[6,7] generated by a current pulse propagated along a wire shaped into a square or helical pattern. The test particle simulations[47] carried out to reconstruct the current pulse time profile give a triangular shape with a ~ 5 ps rise and a ~ 10 ps decay.

The model of electron emission[34] can also be used to predict the duration and the total charge of escaped electrons. We consider a laser pulse with energy $E_l = 40$ J, duration $\tau_l = 1.3$ ps, wavelength $\lambda_l = 1.05$ μm, and focal spot diameter $l = 10$ μm interacting with a $2 \times 2 \times 0.02$ mm^3 gold foil. For these parameters, the hot electron temperature is about 2 MeV and duration of electron emission of about 20 ps is determined by the electron cooling time in the target. This time is consistent with the estimate based on the analysis of the spectra of protons emitted out of the coil. The total charge of escaped electrons calculated with the model is in the range $300 - 450$ nC, depending on the laser absorption coefficient, which also is in qualitative agreement with observations.

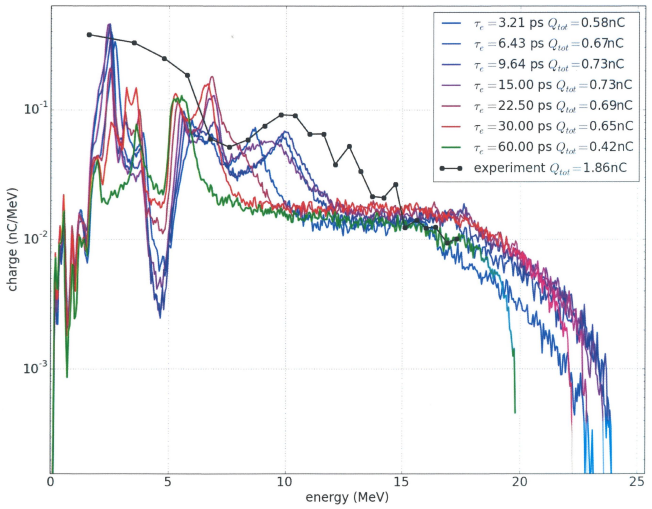

FIG. 9. Comparison of the simulated and measured proton spectra at the end of the coil. The helical coil has a length $L = 15$ mm and a pitch $p = 0.35$.

The so defined electron and proton emission laws were used in a simulation of a helical coil with $p = 0.4$ mm and $L = 8$ mm. Proton spectrum measured at the end of the coil is compared to the spectrum measured in the experiment in Fig. 10(a). A good agreement is found, in particular for the 4 MeV proton peak and the maximum energy around 20 MeV.

Therefore, a combination of experimental results and simulations lead us to infer the electron and proton emission laws from target staying alone. Using these laws, large scale PIC simulations with a real scale target and realistic boundary conditions are able to reproduce the experimental results obtained for various helical coils (see Fig. 10).

IV. PHYSICS OF THE CURRENT PULSE PROPAGATION ALONG THE HELICAL COIL AND ITS EFFECT ON PROTON BUNCHING

Based on this good agreement between simulations and experimental data, a more detailed analysis of the current pulse propagation along the helical coil can be performed. This analysis is completed by an analytical model derived from the traveling wave tube theory[43,49]. In this section, we consider the case of a target with a long helical coil ($L = 15$ mm, $p = 0.35$ mm) described in Secs. II B and III.

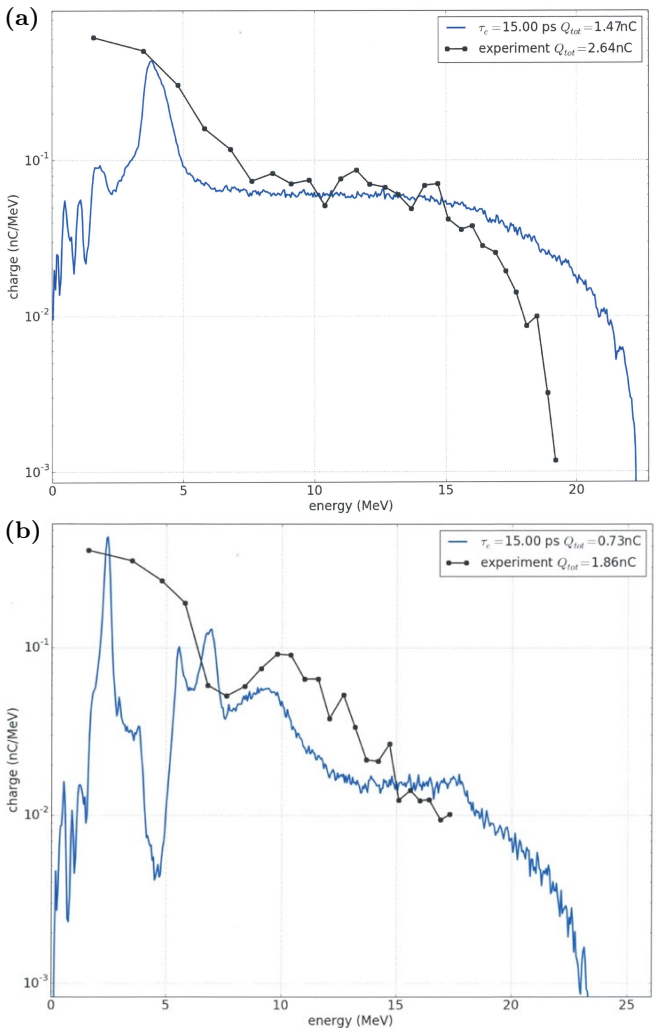

FIG. 10. Comparison of the simulated and measured proton spectra at the end of the coil. The helical coil has a length $L = 8$ mm in panel (a) and 15 mm in panel (b), and a pitch $p = 0.40$ (a) and 0.35 mm (b).

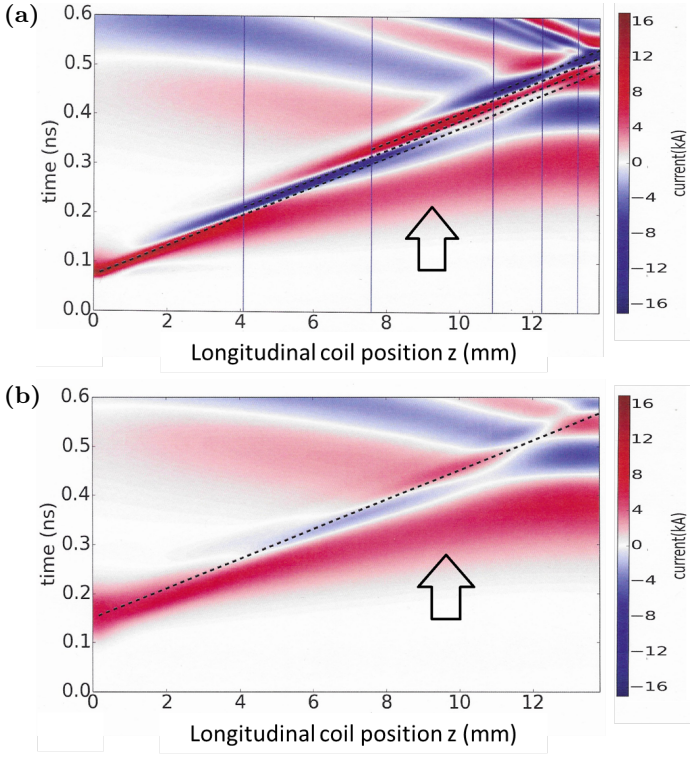

FIG. 11. Comparison of the discharge current pulse propagation along the helical coil axis for an initially short ($\tau_j = 15$ ps) (a) and long ($\tau_j = 60$ ps) (b) electron emission. The helical coil has length $L = 15$ mm and pitch $p = 0.35$ mm.

A. Analysis of large-scale PIC simulations

Figure 11 displays a comparison of the propagation of the discharge current pulse along the coil axis in the cases where the initial duration of the discharge current are $\tau_e = 15$ ps (a) and $\tau_e = 60$ ps (b). From the geometrical considerations, the expected velocity of the current pulse propagation along the coil axis v_0 is given by Eq. (1). The black dashed lines in Fig. 11 represent this constant velocity propagation. One can see that: (i) the velocity of the positive pulse is higher than the one predicted by Eq. (1), and (ii) after $z = 2$ mm, the positive current pulse disperses and its amplitude decreases. At the same time, a negative current pulse is appearing behind it. A major part of this modulation can be explained by the inductive coupling between the neighboring coil turns. In front of the positive pulse, negative currents are not visible in Fig. 11(a) because they are offset by the arriving strong positive pulse. Consequently, the duration of the positive current pulse increases and its intensity decreases with time, while the negative current is reinforced until it becomes dominant after $z = 4$ mm. This phenomenon repeats itself several times for the negative and positive current phases. Each time this phenomenon occurs, the dominant discharge current is delayed. This is shown in Fig. 11(a) by the four black dashed lines. On the contrary, the positive current shown by the black arrow is propagating along the helix axis with a higher velocity than the one predicted by Eq. (1). This means that this positive pulse propagates directly along the coil axis and not along the wire. This is explained by the capacitive coupling between the neighbouring coil turns.

When the discharge current pulse has a longer initial duration of $\tau_e = 60$ ps (Fig. 11(b)), the positive current pulse remains dominant all along the helical coil axis and propagates with a velocity higher than v_0 (see black arrow). So instead of having alternative positive and negative pulses, there is only one positive current pulse. This affects the proton bunching as shown in Fig. 10, where the two peaks around 3 and 10 MeV in the proton spectrum are not observed with this longer initial pulse duration. Thus, negative current pulse plays a key role in the proton bunching.

This role is illustrated in Fig. 12 showing the axial electric field E_z, calculated in the numerical simulations.

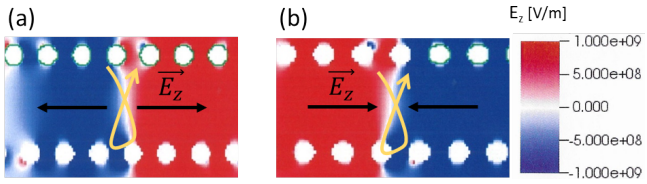

FIG. 12. Distribution of the axial electric field E_z inside the helical coil calculated in the numerical simulations at the positions where the current pulse is positive (a) and negative (b). The z-axis is directed toward the right. The orange arrow represents the location of the current pulse.

For a positive current pulse 12(a), protons are accelerated at the front of the current pulse and decelerated at the back, but for a negative current pulse 12.b, they are decelerated at the front and accelerated at the back. This means that, when the negative current pulse becomes important, protons are bunched. Finally, if the current never becomes negative during its propagation (case for $t_p = 60$ ps), there is no bunch, but if the current becomes several times negative, several bunches appear (case for $t_p = 15$ ps). Therefore, if one wants to get several bunches, it is important to use longer helical coils.

These figures confirm that the intrinsic capacitance and inductance of the helical coil have a strong impact on the discharge current propagation along the coil and therefore on the proton bunching. This new description of the current pulse propagation along the helical coil is confirmed by an analytical model described in the next section.

B. Model of the current pulse propagation along a helical conductor

In this section, we present an analytical model of the current pulse propagation along a helical conductor. This model is derived from works by Pierce[43] and Kino and Paik[49], who have established the dispersion equation for a sheath helical conductor in the frequency domain. We first recall that the propagation of a current J along a linear wire is described by the telegraph equation[55]:

$$\frac{1}{C_0 L_0}\frac{\partial^2 J}{\partial \tau^2} = \frac{R_0}{L_0}\frac{\partial J}{\partial t} + \frac{\partial^2 J}{\partial t^2}, \tag{3}$$

where $\partial\tau$ is an elementary length along the wire and C_0 and L_0 are the wire capacitance and inductance per unit length. As the resistance is neglected in numerical simulations, R_0 is set to zero in the model.

A model of current propagation in helices has been developed in the 1950s for the travelling wave tubes, which are used as electromagnetic wave amplifiers. The sheath helix model has originally been proposed by Pierce[43]. In this model, the helix is considered as a thin cylinder with an anisotropic conductivity, which is non-zero only in the

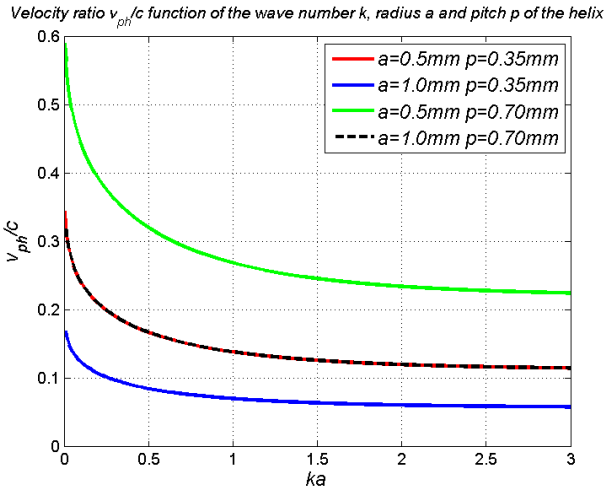

FIG. 13. Dependence of the pulse phase velocity on the wave number obtained from the dispersion equation (4) for helical coils with different radii and pitches.

helical direction. The basic equations of this model were further developed using a circuit approach by Kino and Paik in Ref. 49. The model is set in the Fourier domain assuming that the pulse wave length $2\pi/k$ along the helix axis z is larger than the turn length, $ka \lesssim 1$. Then, the dispersion equation relating the pulse frequency and the wave number $\omega(k)$ reads:

$$\frac{\omega}{kc} = \frac{\beta}{\sqrt{1+\beta^2 D}}, \quad \text{where} \quad D(\gamma a) = \frac{I_1(\gamma a)K_1(\gamma a)}{I_0(\gamma a)K_0(\gamma a)} \tag{4}$$

with $\gamma = (k^2 - \omega^2/c^2)^{1/2}$ and I_n and K_n being the modified Bessel functions of the first and second kind. A relation between the phase velocity $v_{ph} = \omega/k$ and the wave number k is shown in Figure 13. In the limit of $ka \gg 1$, the pulse wavelength is shorter than the turn length, the coupling between turns can be neglected, and pulse propagates with a geometric velocity v_0. By contrast, for longer wavelengths, the capacitive coupling dominates and pulse propagates faster with the phase velocity increasing when approaching asymptotically the light velocity for $ka \to 0$.

Knowing the pulse dispersion $\omega(k)$, one can describe the propagation of the pulse in the Fourier domain by Eq. (5) derived from the telegraph equation (Eq. (3)):

$$\left[\omega^2 - \omega^2(k)\right] J_{k,\omega} = 2ikv_{ph}^2(\omega) J_e(\omega) \tag{5}$$

where the right hand side accounts for the current injection at $z = 0$, at the contact between the foil and the helical coil. Assuming a Gaussian shape of injected pulse $J_e(t) = J_0 \exp(-t^2/2\tau_e^2)$, and by performing the inverse Fourier transform, in frequency and wave number, one can calculate the spatio-temporal profile of the electric

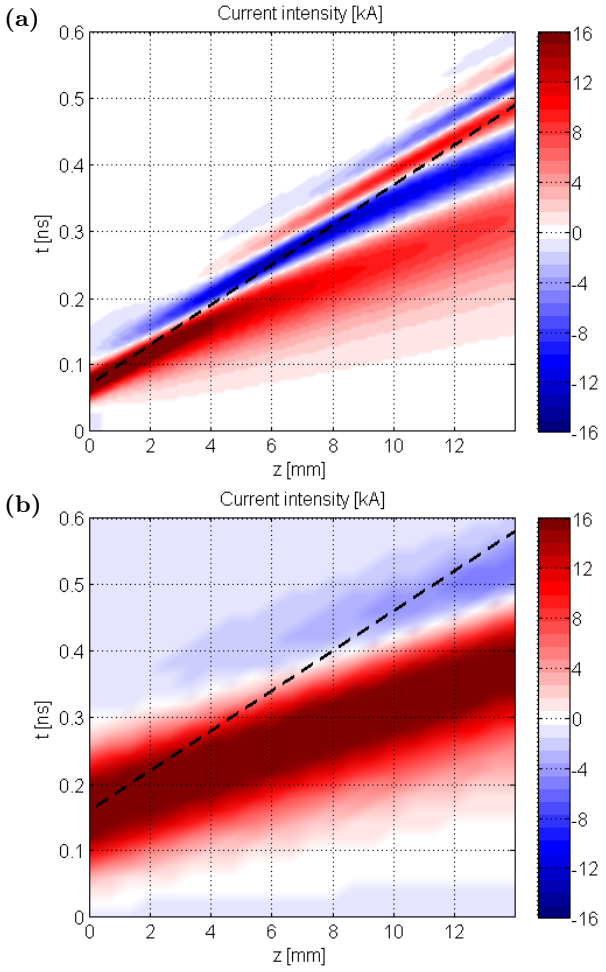

FIG. 14. Model of the current pulse propagation along the helical coil. Comparison for an initially short ($\tau_e = 15$ ps) (a) and long ($\tau_e = 60$ ps) (b) pulse emission. The helical coil has a radius $a = 0.5$ mm and a pitch $p = 0.35$ mm. Figures obtained from the numerical resolution of Eq. (6).

pulse along the helical coil axis. The latter is given by:

$$J(z,t) = \sqrt{\frac{2}{\pi}}\beta c J_0 \tau_e \int_0^{+\infty} \mathrm{d}k \times \frac{\exp[-\omega^2(k)\tau_e^2/2]}{\sqrt{1+\beta^2 D(\gamma(k)a)}} \cos[kz - \omega(k)t]. \quad (6)$$

To compare predictions of this model with the results of numerical simulations shown in Fig. 11, we solve numerically Eq. (6) using the expression (4) for $\omega(k)$.

Figure 14(a) displays the propagation of a discharge current pulse along the coil axis, with the initial duration $\tau_e = 15$ ps. Similarly to Fig. 11(a), we observe that the amplitude of the main pulse decreases during its propagation and that a negative current is induced behind it. This negative current is reinforced with time, and as in Fig. 11(a), the current pulse changes its sign three more times before the end of the coil. Figure 14(b) where $\tau_e = 60$ ps can also be compared to Fig. 11(c). In both figures, the main pulse undergoes much less dispersion and keeps its sign during its propagation along the coil axis. Besides, Fig. 14 confirms that the current pulse is propagating with a higher velocity than the velocity v_0 (2) predicted by the coil geometry (black dashed line).

The results obtained by this model are then in good agreement with the large-scale PIC simulations. It confirms that the current pulse propagates with a dispersion in velocity, which results in modulation of its intensity and generates negative current pulses. It also confirms that the main positive pulse propagates with a velocity higher than v_0. These phenomena must be taken into account in order to obtain a synchronization between the current pulse and protons, and also to obtain the desired proton bunching. Thus, the current propagation model can be helpful in the future helical coils design.

V. DISCUSSION AND CONCLUSION

W have demonstrated the effectiveness of the helical coil devices at high laser energy and intensity. As predicted, the use of high energy laser pulses leads to an increase of the energy cutoff of the proton beam, the number of guided protons (which reach $\sim 10^9$ protons mm^{-2}) and the energy of the proton beam which is of the order of $10-30$ mJ. The proton focusing, post-acceleration and energy selection have been demonstrated at this laser energy level. The use of long (15 mm) helical coils has proven to be interesting for the generation of several proton bunches. We have shown that, at these high laser energies and intensities, the target and helical coil holder must be carefully designed in order to avoid short-circuits.

Large scale numerical simulations have been performed, with realistic material properties, with the 3D PIC code Sophie[48]. We have demonstrated that they can reproduce, with a good agreement, the experimental proton energy distribution at the end of the coil for various helical coil geometries.

Analysis of the numerical simulations allowed to clearly identify the physics of the current pulse propagation along the helical coil and its effect on the proton bunching. The source of the chromatic focusing, post-acceleration and bunching is the discharge current pulse generated by the charge ejection from the target. This current propagates along the helical coil and produces an electromagnetic pulse inside and outside the helical structure, which acts on the proton beam. Contrary to what has been described in the past publications[30,35–37,44,45], we have demonstrated that the current pulse does not propagate with a constant phase velocity calculated from the coil geometry (1), but that it is dispersed in velocity due to the frequency dependence of the capacitance and inductance of the helical coil. This dispersion modulates the current intensity during its propagation along the helical coil, negative current pulses appear and lead to a favorable configuration of the longitudinal electric

field for the proton bunching. Therefore, several proton bunches can be formed using long helical coils. Each current pulse propagates with a velocity greater than the one calculated from the coil geometry (1). This must be taken into account in order to obtain a synchronization between the current pulse propagation and the protons.

We have confirmed this propagation process by its comparison with an analytical model of the current pulse propagation along a helical conductor[43,49], which is in good agreement with the PIC simulations. This current propagation model can be useful in the future helical coils design and optimization. These results are of interest for the further experiments with optimized coils where the discharge current velocity can be adjusted to proton bunches of prescribed energy.

The use of helical coils opens up the possibility to transport high flux quasi-monoenergetic proton beams to distant targets. A larger distance between the proton source and the target is interesting for experiments for isotope production, isochoric heating or ion driven fast ignition. This device can also be improved by using curved targets to control the proton flux injected in the coil or structured targets to increase laser absorption and efficiency of proton acceleration.

Appendix A: Proton spectra obtained from the analysis of the dose deposition in the RCF stacks

The RCF stacks used in this experimental campaign were composed of HD-V2 (Gafchromic^{TM}) films and two 10 μm thick aluminium foil at the front to stop the major part of X rays and hot electrons. These films are made of a $\lesssim$ 100-μm-thick polyester substrate and few-μm-thick active layer. A few weeks after the experiment, the films of the stack were scanned with a transparency acquisition and a high resolution (600 dpi).

For each RCF stack, and for each laser shot, the procedure to obtain the absolute proton spectrum is the following.

The optical density (OD) is firstly calculated for each film j and each canal c (red [R], green [G], blue [B]) :

$$OD_{c,j}(x,y) = \log_{10} \frac{I_{c,j}(x,y)}{I_{c,0}} \tag{A1}$$

where (x,y) is a point at the surface of the film j, $I_{c,0} = \max I_{c,0}(x,y)$ is the maximum transparency of a chosen film which has not been irradiated. We choose to use the sum optical density $OD_s = \sum_c OD_c$ because of good sensitivity at low dose deposition and no saturation at high dose deposition. We then calculate the fluence for each film j:

$$F_j(x,y) = \begin{cases} f(DO_{s,j}(x,y)) & \text{if } OD_{s,j}(x,y) > OD_{th} \\ 0 & \text{if } OD_{s,j}(x,y) \leqslant OD_{th} \end{cases} \tag{A2}$$

where $OD_{th} = 10^{-3}$ is the chosen threshold optical density under which any signal is considered as noise and f is a function transferring the optical density to the fluence. This function has been calibrated by irradiating other RCF to known doses on a radio-frequency particle accelerator.

For a given aperture angle α of interest, the fluence is integrated over the corresponding circular surface $S = \pi(d_{TCC-RCF} \tan\alpha)^2$, where $d_{TCC-RCF}$ is the distance between the proton source and the RCF stack, to obtain the total deposited proton energy $E_{dep,j}$ on each film j

$$E_{dep,j} = \iint_S F_j(x,y)\,\mathrm{d}x\,\mathrm{d}y. \tag{A3}$$

The Monte Carlo code GEANT4 (GEometry ANd Tracking)[57] is used to calculate the matrix which gives the energy loss $e_{k,j}$ of each proton with the initial energy $E_{p,k}$ in each film j of the stack. The total deposited energy in each film j (A3) then writes:

$$E_{dep,j} = \sum_k e_{k,j} N_k \tag{A4}$$

where N_k is the number of protons with initial energy $E_{p,k}$. Besides, each film j can be associated to the energy $E_j = E_{p,j}$ of protons which deposit most of the energy in it. The location of this film in the stack corresponds to the position of the Bragg peak of the corresponding proton. Then, by using a deconvolution algorithm which inverts Eq. (A4), the proton distribution (E_j, N_j) and the proton spectrum $\mathrm{d}N_p/dE$ are obtained.

ACKNOWLEDGMENTS

The two first authors have equally contributed to the writing of this paper.

The authors are grateful to L. Perrachon for the first numerical simulations that she has performed during her internship. The authors are grateful to N. Blanchot, B. Cassani, O. Cessenat, X. Davoine, J. Gardelle, A. Michau and D. Raffestin for their help and useful discussions.

This work is supported by the CEA/DAM laser-plasma experiments validation project and the CEA/DAM basic technical and scientific studies project. It is also partly supported by the exploratory program Bottom-Up lead by the Commissariat à l'Énergie Atomique et aux Energies Alternatives (CEA). This study has been also carried out with financial support from the French National Agency of Research, Contract No. ANR-10-EQPX-0048 and Programme IdEx Bordeaux-LAPHIA (ANR-10-IDEX-03-02).

REFERENCES

[1] H. Daido, M. Nishiuchi, A. S. Pirozhkov, Rep. Progress Phys. **75** (2012) 056401.

[2]A. Macchi, M. Borghesi, M. Passoni, Rev. Mod. Phys. **85** (2013) 751.
[3]P. K. Patel, A. J. Mackinnon, M. H. Key, T. E. Cowan, M. E. Foord, M. Allen, D. F. Price, H. Ruhl, P. T. Springer, R. Stephens, Phys. Rev. Lett. **91** (2003) 125004.
[4]K. Nemoto, A. Maksimchuk, S. Banerjee, K. Flippo, G. Mourou, D. Umstadter, V. Yu. Bychenkov, Appl. Phys. Lett. **78** (2001) 595.
[5]K. L. Lancaster, S. Karsch, H. Habara, F. N. Beg, E. L. Clark, R. Freeman, M. H. Key, J. A. King, R. Kodama, K. Krushelnick, K. W. D. Ledingham, P. McKenna, C. D. Murphy, P. A. Norreys, R. Stephens, C. Stöeckl, Y. Toyama, M. S. Wei, M. Zepf, Phys. Plasmas **11** (2004) 3404.
[6]M. Borghesi, A. Schiavi, D. H. Campbell, M. G. Haines, O. Willi, A. J. MacKinnon, L. A. Gizzi, M. Galimberti, R. J. Clarke, H. Ruhl, Plasma Phys. Control. Fusion **43** (2001) A267.
[7]M. Borghesi, L. Romagnani, A. Schiavi, D. H. Campbell, M. G. Haines, O. Willi, A. J. Mackinnon, M. Galimberti, L. Gizzi, R. J. Clarke, S. Hawkes, Appl. Phys. Lett. **82** (2003) 1529.
[8]M. Roth, T. E. Cowan, M. H. Key, S. P. Hatchett, C. Brown, W. Fountain, J. Johnson, D. M. Pennington, R. A. Snavely, S. C. Wilks, K. Yasuike, H. Ruhl, F. Pegoraro, S. V. Bulanov, E. M. Campbell, M. D. Perry, H. Powell, Phys. Rev. Lett. **86** (2001) 436.
[9]V. Y. Bychenkov, W. Rozmus, A. Maksimchuk, D. Umstadter, C. E. Capjack, Plasma Phys. Rep. **27** (2001) 1017.
[10]V. Malka, S. Fritzler, E. Lefebvre, E. d'Humières, R. Ferrand, G. Grillon, C. Albaret, S. Meyroneinc, J.-P. Chambaret, A. Antonetti, D. Hulin, Med. Phys. **31** (2004) 1587.
[11]R. A. Snavely, M. H. Key, S. P. Hatchett, T. E. Cowan, M. Roth, T. W. Phillips, M. A. Stoyer, E. A. Henry, T. C. Sangster, M. S. Singh, S. C. Wilks, A. MacKinnon, A. Offenberger, D. M. Pennington, K. Yasuike, A. B. Langdon, B. F. Lasinski, J. Johnson, M. D. Perry, E. M. Campbell, Phys. Rev. Lett. **85** (2000) 2945.
[12]S. C. Wilks, A. B. Langdon, T. E. Cowan, M. Roth, M. Singh, S. Hatchett, M. H. Key, D. Pennington, A. MacKinnon, R. A. Snavely, Phys. Plasmas **8** (2001) 542.
[13]H. Schwoerer, S. Pfotenhauer, O. Jäckel, K.-U. Amthor, B. Liesfeld, W. Ziegler, R. Sauerbrey, K. W. D. Ledingham, T. Esirkepov, Nature **439** (2006) 445.
[14]R. A. Snavely, B. Zhang, K. Akli, Z. Chen, R. R. Freeman, P. Gu, S. P. Hatchett, D. Hey, J. Hill, M. H. Key, Y. Izawa, J. King, Y. Kitagawa, R. Kodama, A. B. Langdon, B. F. Lasinski, A. Lei, A. J. MacKinnon, P. Patel, R. Stephens, M. Tampo, K. A. Tanaka, R. Town, Y. Toyama, T. Tsutsumi, S. C. Wilks, T. Yabuuchi, and J. Zheng, Phys. Plasmas **14** (2007) 092703.
[15]S. Kar, K. Markey, P. T. Simpson, C. Bellei, J. S. Green, S. R. Nagel, S. Kneip, D. C. Carroll, B. Dromey, L. Willingale, E. L. Clark, P. McKenna, Z. Najmudin, K. Krushelnick, P. Norreys, R. J. Clarke, D. Neely, M. Borghesi, and M. Zepf, Phys. Rev. Lett. **100** (2008) 105004.
[16]S. Kar, K. Markey, M. Borghesi, D. C Carroll, P. McKenna, D. Neely, M. N. Quinn, and M. Zepf, Phys. Rev. Lett. **106** (2011) 225003.
[17]T. Bartal, M. E. Foord, C. Bellei, M. H. Key, K. A. Flippo, S. A. Gaillard, D. T. Offermann, P. K. Patel, L. C. Jarrott, D. P. Higginson, M. Roth, A. Otten, D. Kraus, R. B. Stephens, H. S. McLean, E. M. Giraldez, M. S. Wei, D. C. Gautier, F. N. Beg, Nature Phys. **8** (2011) 139.
[18]M. Burza, A. Gonoskov, G. Genoud, A. Persson, K. Svensson, M. Quinn, P. McKenna, M. Marklund, C.-G. Wahlström, New J. Phys. **13** (2011) 013030.
[19]S. N. Chen, E. d'Humières, E. Lefebvre, L. Romagnani, T. Toncian, P. Antici, P. Audebert, E. Brambrink, C. A. Cecchetti, T. Kudyakov, A. Pipahl, Y. Sentoku, M. Borghesi, O. Willi, J. Fuchs, Phys. Rev. Lett. **108** (2012) 055001.
[20]M. Schollmeier, S. Becker, M. Geißel, K. A. Flippo, A. Blažević, S. A. Gaillard, D. C. Gautier, F. Grüner, K. Harres, M. Kimmel, F. Nürnberg, P. Rambo, U. Schramm, J. Schreiber, J. Schütrumpf, J. Schwarz, N. A. Tahir, B. Atherton, D. Habs, B. M. Hegelich, M. Roth, Phys. Rev. Lett. **101** (2008) 055004.
[21]S. Ter-Avetisyan, M. Schnürer, R. Polster, P. V. Nickles, W. Sandner, Laser Part. Beams **26** (2008) 637.
[22]M. Nishiuchi, I. Daito, M. Ikegami, H. Daido, M. Mori, S. Orimo, K. Ogura, A. Sagisaka, A. Yogo, A. S. Pirozhkov, H. Sugiyama,, H. Kiriyama, H. Okada, S. Kanazawa, S. Kondo, T. Shimomura, M. Tanoue, Y. Nakai, H. Sasao, D. Wakai, H. Sakaki, P. Bolton, I. W. Choi, J. H. Sung, J. Lee, Y. Oishi, T. Fujii, K. Nemoto, H. Souda, A. Noda, Y. Iseki, T. Yoshiyuki , Appl. Phys. Lett. **94** (2009) 061107.
[23]K. Harres, I. Alber, A. Tauschwitz, V. Bagnoud, H. Daido, M. Günther, F. Nürnberg, A. Otten, M. Schollmeier, J. Schütrumpf, M. Tampo, and M. Roth, Phys. Plasmas **17** (2010) 023107.
[24]S. Busold, D. Schumacher, O. Deppert, C. Brabetz, S. Frydrych, F. Kroll, M. Joost, H. Al-Omari, A. Blažević, B. Zielbauer, I. Hofmann, V. Bagnoud, T. E. Cowan, M. Roth, Phys. Rev. ST Accel. Beams **16** (2013) 101302.
[25]T. Toncian, M. Borghesi, J. Fuchs, E. d'Humières, P. Antici, P. Audebert, E. Brambrink, C. A. Cecchetti, A. Pipahl, L. Romagnani, O. Willi, Science **312** (2006) 410.
[26]K. Krushelnick, E. L. Clark, R. Allott, F. N. Beg, C. N. Danson, A. Machacek, V. Malka, Z. Najmudin, D. Neely, P. A. Norreys, M. R. Salvati, M. I. K. Santala, M. Tatarakis, I. Watts, M. Zepf, A. E. Dangor, IEEE Trans. Plasma Sci. **28** (2000) 1110.
[27]S. Nakamura, M. Ikegami, Y. Iwashita, T. Shirai, H. Tongu, H. Souda, H. Daido, M. Mori, M. Kado, A. Sagisaka, K. Ogura, M. Nishiuchi, S. Orimo, Y. Hayashi, A. Yogo, A. S. Pirozhkov, S. V. Bulanov, T. Esirkepov,

A. Nagashima, T. Kimura, T. Tajima, T. Takeuchi, A. Fukumi, Z. Li, A. Noda, Jap. J. Appl. Phys. **46** (2007) L717.
[28]P. Antici, M. Migliorati, A. Mostacci, L. Picardi, L. Palumbo, C. Ronsivalle, Phys. Plasmas **18** (2011) 073103.
[29]D. Jahn, D. Schumacher, C. Brabetz, F. Kroll, F. E. Brack, J. Ding, R. Leonhardt, I. Semmler, A. Blažević, U. Schramm, M. Roth, Phys. Rev. Accel. Beams **22** (2019) 011301.
[30]S. Kar, H. Ahmed, R. Prasad, M. Cerchez, S. Brauckmann, B. Aurand, G. Cantono, P. Hadjisolomou, C. L. S. Lewis, A. Macchi, G. Nersisyan, A. P. L. Robinson, A. M. Schroer, M. Swantusch, M. Zepf, O. Willi, M. Borghesi, Nature Comm. **7** (2016) 10792.
[31]K. B. Wharton, S. P. Hatchett, S. C. Wilks, M. H. Key, J. D. Moody, V. Yanovsky, A. A. Offenberger, B. A. Hammel, M. D. Perry, C. Joshi, Phys. Rev. Lett. **81** (1998) 822.
[32]J.-L. Dubois, F. Lubrano-Lavaderci, D. Raffestin, J. Ribolzi, J. Gazave, A. Compant La Fontaine, E. d'Humières, S. Hulin, Ph. Nicolaï, A. Poyé, V. T. Tikhonchuk, Phys. Rev. E **89** (2014) 013102.
[33]A. Poyé, J.-L. Dubois, F. Lubrano-Lavaderci, E. D'Humières, M. Bardon, S. Hulin, M. Bailly-Grandvaux, J. Ribolzi, D. Raffestin, J. J. Santos, Ph. Nicolaï, V. Tikhonchuk, Phys. Rev. E **92** (2015) 043107.
[34]A. Poyé, S. Hulin, J. Ribolzi, M. Bailly-Grandvaux, F. Lubrano-Lavaderci, M. Bardon, D. Raffestin, J. J. Santos, V. Tikhonchuk, Phys. Rev. E **98** (2018) 033201.
[35]S. Kar, H. Ahmed, G. Nersisyan, S. Brauckmann, F. Hanton, A. L. Giesecke, K. Naughton, O. Willi, C. L. S. Lewis, M. Borghesi, Phys. Plasmas **23** (2016) 055711.
[36]H. Ahmed, S. Kar, G. Cantono, G. Nersisyan, S. Brauckmann, D. Doria, D. Gwynne, A. Macchi, K. Naughton, O. Willi, C.L.S. Lewis, M. Borghesi, Nucl. Instrum. Meth. A **829** (2016) 172.
[37]H. Ahmed, S. Kar, A.L. Giesecke, D. Doria, G. Nersisyan, O. Willi, C.L.S. Lewis and M. Borghesi, High Power Laser Sci. Eng. **5** (2017) e4.
[38]E. Aktan, H. Ahmed, B. Aurand, M. Cerchez, A. Poyé, P. Hadjisolomou, M. Borghesi, S. Kar, O. Willi, R. Prasad, Phys. Plasmas **26** (2019) 070701.
[39]A. Poyé, S. Hulin, M. Bailly-Grandvaux, J.-L. Dubois, J. Ribolzi, D. Raffestin, M. Bardon, F. Lubrano-Lavaderci, E. D'Humières, J. J. Santos, Ph. Nicolaï, V. Tikhonchuk, Phys. Rev. E **91** (2015) 043106.
[40]F. Consoli, V. T. Tikhonchuk, M. Bardon, P. Bradford, D. C. Carroll, J. Cikhardt, M. Cipriani, R. J. Clarke, T. E. Cowan, C. N. Danson, R. De Angelis, M. De Marco, J.-L. Dubois, B. Etchessahar, A. Laso Garcia, D. I. Hillier, A. Honsa, W. Jiang, V. Kmetik, J. Krása, Y. Li, F. Lubrano, P. McKenna, J. Metzkes-Ng, A. Poyé, I. Prencipe, P. Rączka, R. A. Smith, R. Vrana, N. C. Woolsey, E. Zemaityte, Y. Zhang, Z. Zhang, B. Zielbauer, D. Neely, High Power Laser Sci. Eng. **8** (2020) e22.
[41]D. R. Chick, D. P. R. Petrie, Nature **4279** (1951) 782.
[42]D. R. Chick, D. P. R. Petrie, D. G. Keith-Walker, H. Longley, Nature **4583** (1957) 432.
[43]J. R. Pierce, Travelling Wave Tubes (D. Van Nostrand Company, Inc., Princeton, New Jersey, 1950).
[44]H. Ahmed, S. Kar, G. Cantono, P. Hadjisolomou, A. Poye, D. Gwynne, C. L. S. Lewis, A. Macchi, K. Naughton, G. Nersisyan, V. Tikhonchuk, O. Willi M. Borghesi, Sci. Rep. **7** (2017) 10891.
[45]H. Ahmed, S. Kar, G. Cantono, D. Doria, A.L. Giesecke, D. Gwynne, C.L.S. Lewis, A. Macchi, G. Nersisyan, K. Naughton, O. Willi, M. Borghesi, J. Instrum. **12** (2017) C06025.
[46]K. Jiang, C. T. Zhou, T. W. Huang, L. B. Ju, C. N. Wu, L. Li, H. Zhang, S. Z. Wu, T. X. Cai, B. Qiao, Plasma Phys. Control. Fusion **61** (2019) 075004.
[47]L. Romagnani, M. Borghesi, C.A. Cecchetti, S. Kar, P. Antici, P. Audebert, S. Bandhoupadjay, F. Ceccherini, T. Cowan, J. Fuchs, M. Galimberti, L.A. Gizzi, T. Grismayer, R. Heathcote, R. Jung, T.V. Liseykina, A. Macchi, P. Mora, D. Neely, M. Notley, J. Osterholtz, C.A. Pipahl, G. Pretzler, A. Schiavi, G. Schurtz, T. Toncian, P.A. Wilson and O. Willi, Laser Part. Beams **26** (2008) 241 and references therein.
[48]O. Cessenat, arXiv (2013) 1301.4539.
[49]G. S. Kino, S. F. Paik, J. Appl. Phys. **33** (1962) 3002. Eq. (24)
[50]Laboratoire pour l'Utilisation des Lasers Intenses. LULI2000 [Online]. https://portail.polytechnique.edu/luli/fr/installations/luli2000 [April 2020].
[51]National Institute of Standards and Technology. PSTAR : Stopping Power and Range Tables for Protons [Online]. 1998. https://physics.nist.gov/PhysRefData/Star/Text/PSTAR.html [April 2020].
[52]M. Bardon, B. Etchessahar, F. Lubrano, S. Bazzoli, M. Ferri, J. Ribolzi, P. Mirabel, A. Compant La Fontaine, N. Mallejac, S. Cadra, L. Chaigne, S. Depierreux, J. Baggio, N. Blanchot, G. Birindelli, A. Casner, V. T. Tikhonchuk, Phys. Rev. Res. **X** (2020) XXX.
[53]M. Borghesi, A. J. Mackinnon, D. H. Campbell, D. G. Hicks, S. Kar, P. K. Patel, D. Price, L. Romagnani, A. Schiavi, O. Willi, Phys. Rev. Lett. **92** (2004) 055003.
[54]L. Romagnani, J. Fuchs, M. Borghesi, P. Antici, P. Audebert, F. Ceccherini, T. Cowan, T. Grismayer, S. Kar, A. Macchi, P. Mora, G. Pretzler, A. Schiavi, T. Toncian, O. Willi, Phys. Rev. Lett. **95** (2005) 195001.
[55]S. Ramo, J. R. Whinnery and T. van Duzer, Fields and Waves in Communication Electronics (New York: John Wiley & Sons, 1965).
[56]F. R. Zypman, Am. J. Phys. **74** (2006) 295.
[57]Geant4 Collaboration, Nucl. Instr. Meth A **506** (2003) 250.